# Supplementary material for "Collapse of microbubbles over an elastoplastic wall"

Dario Abbondanza, Mirko Gallo, and Carlo Massimo Casciola

Dipartimento di Ingegneria Meccanica e Aerospaziale, Sapienza Università di Roma,
Via Eudossiana 18 00184 Roma, Italy.

## 1   Numerical formulation for the Navier-Stokes equations

### 1.1   Weak form

The Navier-Stokes equations with capillarity (see §3 in the manuscipt)

$$\frac{\partial \rho}{\partial t} + \nabla \cdot (\rho \mathbf{u}) = 0, \tag{S1a}$$

$$\frac{\partial \rho \mathbf{u}}{\partial t} + \nabla \cdot (\rho \mathbf{u} \otimes \mathbf{u}) = \nabla \cdot T, \tag{S1b}$$

$$\frac{\partial E}{\partial t} + \nabla \cdot (E \mathbf{u}) = \nabla \cdot (T \cdot \mathbf{u}) - \nabla \cdot \mathbf{q}_f. \tag{S1c}$$

with constitutive relations

$$\mathbf{T} = - \left( p_0 - \frac{\lambda}{2} |\nabla \rho|^2 - \rho \nabla \cdot (\lambda \nabla \rho) \right) \mathbf{I} +$$
$$- \lambda \nabla \rho \otimes \nabla \rho + \eta (\nabla \mathbf{u} + (\nabla \mathbf{u})^T) - \tilde{\eta}(\nabla \cdot \mathbf{u}) \mathbf{I}, \tag{S2}$$

$$\mathbf{q}_f = \lambda \rho \nabla \rho \nabla \cdot \mathbf{u} - k \nabla \theta, \tag{S3}$$

have been solved numerically to obtain the results presented in the manuscript. They are discretised by adopting the finite element method and are then implemented numerically using the library deal.II [6], which provides support for automatic grid refinement, that has been exploited in this work. By defining an auxiliary variable $g = \nabla^2 \rho$, the system of Eqs. (S1) can be rewritten as

$$\frac{\partial \mathbf{U}}{\partial t} + \nabla \cdot \mathbf{F}(\mathbf{U}, \nabla \mathbf{U}, g) = \mathbf{0}, \tag{S4}$$

$$g = \nabla^2 \rho, \tag{S5}$$

with

$$\mathbf{U} = \begin{pmatrix} \rho \\ \rho \mathbf{u} \\ E \end{pmatrix}, \qquad \mathbf{F} = \begin{pmatrix} \rho \mathbf{u} \\ \rho \mathbf{u} \otimes \mathbf{u} - \mathbf{T} \\ E \mathbf{u} - T \cdot \mathbf{u} + \mathbf{q}_f \end{pmatrix}. \tag{S6}$$

Using the following notation to shortly indicate the integral of the product of two functions over the simulation domain,

$$(f, g)_{\Omega_f} = \int_{\Omega_f} fg \, d\mathbf{x}, \tag{S7}$$

it's possible to rewrite Eq. (S4) in weak form:

$$\left( \frac{\partial \mathbf{U}}{\partial t}, \mathbf{\Phi} \right)_{\Omega_f} - (\mathbf{F}, \nabla \mathbf{\Phi})_{\Omega_f} + (\mathbf{F} \cdot \hat{\mathbf{n}}, \mathbf{\Phi})_{\partial \Omega_f} = \mathbf{0}, \tag{S8}$$

having chosen appropriate test functions $\mathbf{\Phi}$ with the required regularity. Discretizing Eq. (S8) in time using the Crank-Nicolson method, and having in mind the prescribed boundary conditions (Eq. (6.1) in the manuscript),

$$\mathbf{u} = 0, \qquad \mathbf{q}_f \cdot \hat{\mathbf{n}} = 0, \qquad \frac{\partial \rho}{\partial n} = 0 \quad \text{on } \partial \Omega_f, \tag{S9}$$

we can drop the boundary term $(\mathbf{F} \cdot \hat{\mathbf{n}}, \boldsymbol{\Phi})_{\partial \Omega_f} = \mathbf{0}$ in Eq. (S8) and obtain

$$(\mathbf{U}_{n+1}, \boldsymbol{\Phi})_{\Omega_f} - (\mathbf{U}_n, \boldsymbol{\Phi})_{\Omega_f} - \frac{\Delta t}{2} \left[ (\mathbf{F}_{n+1}, \nabla \boldsymbol{\Phi})_{\Omega_f} + (\mathbf{F}_n, \nabla \boldsymbol{\Phi})_{\Omega_f} \right] = \mathbf{0}, \tag{S10}$$

where $\mathbf{F}_n = \mathbf{F}(\mathbf{U}_n, \nabla \mathbf{U}_n, g_n)$. Adopting the Newton-Raphson iteration scheme, with residual

$$\Psi_{n+1} = (\mathbf{U}_{n+1}, \boldsymbol{\Phi})_{\Omega_f} - (\mathbf{U}_n, \boldsymbol{\Phi})_{\Omega_f} - \frac{\Delta t}{2} \left[ (\mathbf{F}_{n+1}, \nabla \boldsymbol{\Phi})_{\Omega_f} + (\mathbf{F}_n, \nabla \boldsymbol{\Phi})_{\Omega_f} \right], \tag{S11}$$

and linearizing it around the $k$-th iteration and solving for

$$\Psi_{n+1}^{k+1} \approx \Psi_{n+1}^k + \left. \frac{\partial \Psi}{\partial \mathbf{U}} \right|_{n+1}^k (\mathbf{U}_{n+1}^{k+1} - \mathbf{U}_{n+1}^k) = 0, \tag{S12}$$

we get the system of linear equations to be solved:

$$\left( \delta \mathbf{U}_{n+1}^k, \boldsymbol{\Phi} \right)_{\Omega_f} - \frac{\Delta t}{2} \left( \left. \frac{\partial \mathbf{F}}{\partial \mathbf{U}} \right|_{n+1}^k \delta \mathbf{U}_{n+1}^k, \nabla \boldsymbol{\Phi} \right)_{\Omega_f} = \tag{S13}$$

$$- \left( \mathbf{U}_{n+1}^k, \boldsymbol{\Phi} \right)_{\Omega_f} + (\mathbf{U}_n, \boldsymbol{\Phi})_{\Omega_f} + \frac{\Delta t}{2} \left[ \left( \mathbf{F}_{n+1}^k, \nabla \boldsymbol{\Phi} \right)_{\Omega_f} + (\mathbf{F}_n, \nabla \boldsymbol{\Phi})_{\Omega_f} \right], \tag{S14}$$

where we denoted $\delta \mathbf{U}_{n+1}^k = \mathbf{U}_{n+1}^{k+1} - \mathbf{U}_{n+1}^k$.

The spatial discretization adopted in this work considers the simulation domain $\Omega_f$ as composed of $N_{cells}$ non-overlapping cells $\Omega_f^h$ which are sufficient to cover the whole domain, $\Omega_f = \cup^{N_{cells}} \Omega_f^h$. On each cell, the test functions $\boldsymbol{\Phi}$ take the form of appropriate shape functions. In particular, in the present work, piecewise linear shape functions are adopted, and we assume that it is possible to represent the solution $\mathbf{U}(\mathbf{x}, t)$ as a linear combination of the shape functions through the nodal values $\tilde{\mathbf{U}}_i(t)$, such that

$$\mathbf{U}(\mathbf{x}, t) = \sum_i^{n_{nodes}} \tilde{\mathbf{U}}_i(t) \boldsymbol{\Phi}_i(\mathbf{x}), \tag{S15}$$

and Eq. (S13) reads

$$\left[ (\boldsymbol{\Phi}_i, \boldsymbol{\Phi}_j)_{\Omega_f^h} - \frac{\Delta t}{2} \left( \left. \frac{\partial \mathbf{F}}{\partial \mathbf{U}} \right|_{n+1}^k \boldsymbol{\Phi}_i, \nabla \boldsymbol{\Phi}_j \right)_{\Omega_f^h} \right] \delta \tilde{\mathbf{U}}_{n+1, i}^k = \tag{S16}$$

$$- \left( \mathbf{U}_{n+1}^k, \boldsymbol{\Phi}_j \right)_{\Omega_f^h} + (\mathbf{U}_n, \boldsymbol{\Phi}_j)_{\Omega_f^h} + \frac{\Delta t}{2} \left[ \left( \mathbf{F}_{n+1}^k, \nabla \boldsymbol{\Phi}_j \right)_{\Omega_f^h} + (\mathbf{F}_n, \nabla \boldsymbol{\Phi}_j)_{\Omega_f^h} \right]. \tag{S17}$$

## 1.2 Unstructured grid treatment and refinement

As mentioned in the previous section and in the manuscript (see § 5), we exploited automatic grid refinement capabilities offered by the deal.II library. The diffuse interface model outlined in the paper is a phase field model that requires very high resolution in the interfacial region, which is of the order of new nanometers at the ambient temperature for a liquid-vapour system. This makes the simulation of a microbubble a very complicated and computationally demanding multiscale problem. In our numerical implementation, a cell is refined or coarsen based on the Kelly error estimator (Ainsworth and Oden 2011; Kelly et al. 1983), which approximates the error per cell by integration of the jump of the gradient of the solution across the faces of each cell, and it is based on the analysis of the generalized Poisson equation $-\nabla \cdot (a(x)\nabla u) = 0$, with either Dirichlet or Neumann boundary conditions. At each timestep of the numerical scheme introduced in the previous sections, the error per cell is computed, and a certain amount of cells with higher/lower error are refined/coarsen. This procedure is not applied to the whole solution vector, since numerical experiments have shown that the best convergence and stability of the solution is achieved when the whole mesh is refined according to the density field only.

The unstructured computational grid is adaptevely refined during the simulations, starting from an initial maximum resolution at the liquid/vapour interface of $\Delta = \Delta r = \Delta z = L/2^{15}$ and an initial minimum resolution in the external liquid of $\Delta = L/2^6$ (being $L = 20R_0$ the radial domain
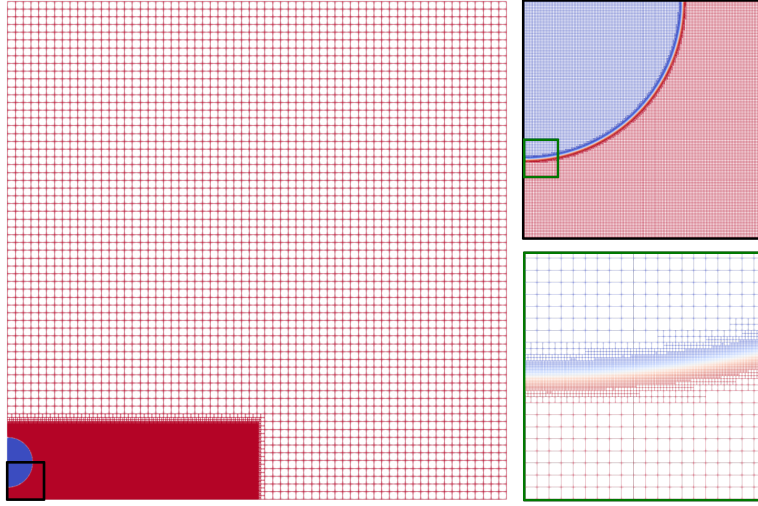
Figure 1: Initial condition of the fluid simulation with grid wireframe, where the three resolution levels are clearly visible.
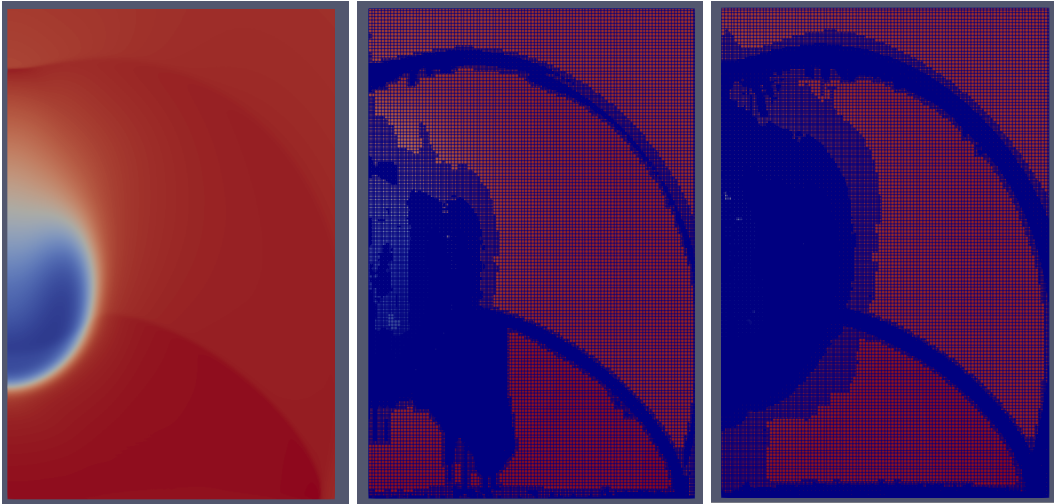


Figure 2: Left panel: Density field. Center panel: instantaneous grid (minimum grid spacing $\Delta = L/2^{15}$). Right panel: refined instantaneous grid (minimum grid spacing $\Delta = L/2^{16}$). Snapshot taken during the collapse phase.

extension), see Figure 1. To appropriately resolve the dynamics of the bubble, and accurately follow the pressure/shock wave at the wall, a portion of the domain $\Omega_{f,res} = [0, L/2] \times [0, H_{res}]$ is forced to maintain a minimum grid resolution of $\Delta = L/2^{11}$. The time step $\Delta t$ ranges between $10^{-5}$ and $10^{-3}$ (dimensionless units), depending on the collapse phase and initial overpressure $\beta$. An example of how the grid is capable of adapting and follow the liquid/vapour interface and the shock wave dynamics is apparent in Figure 2, where the effect of refining the adaptive grid is also shown. Shock capturing was not required since the grid resolution is sufficient to resolve the shock front directly.

## 1.3 Convergence study

To ensure that the results obtained are grid independent, we ran additional tests doubling the maximum resolution allowed during the simulation (i.e., decreasing the minimum grid spacing from $\Delta = L/2^{15}$ to $\Delta = L/2^{16}$). Figure 3 compares the bubble volume evolution, the maximum stress recorded at the wall during time, and the pressure profiles at the wall for the two grids. Figure 4 provides a comparison of two snapshots of density and temperature fields across the collapse time $t/T_c^w = 1$. Finally, Figure 2 above directly compares the coarse and fine adaptive grids.
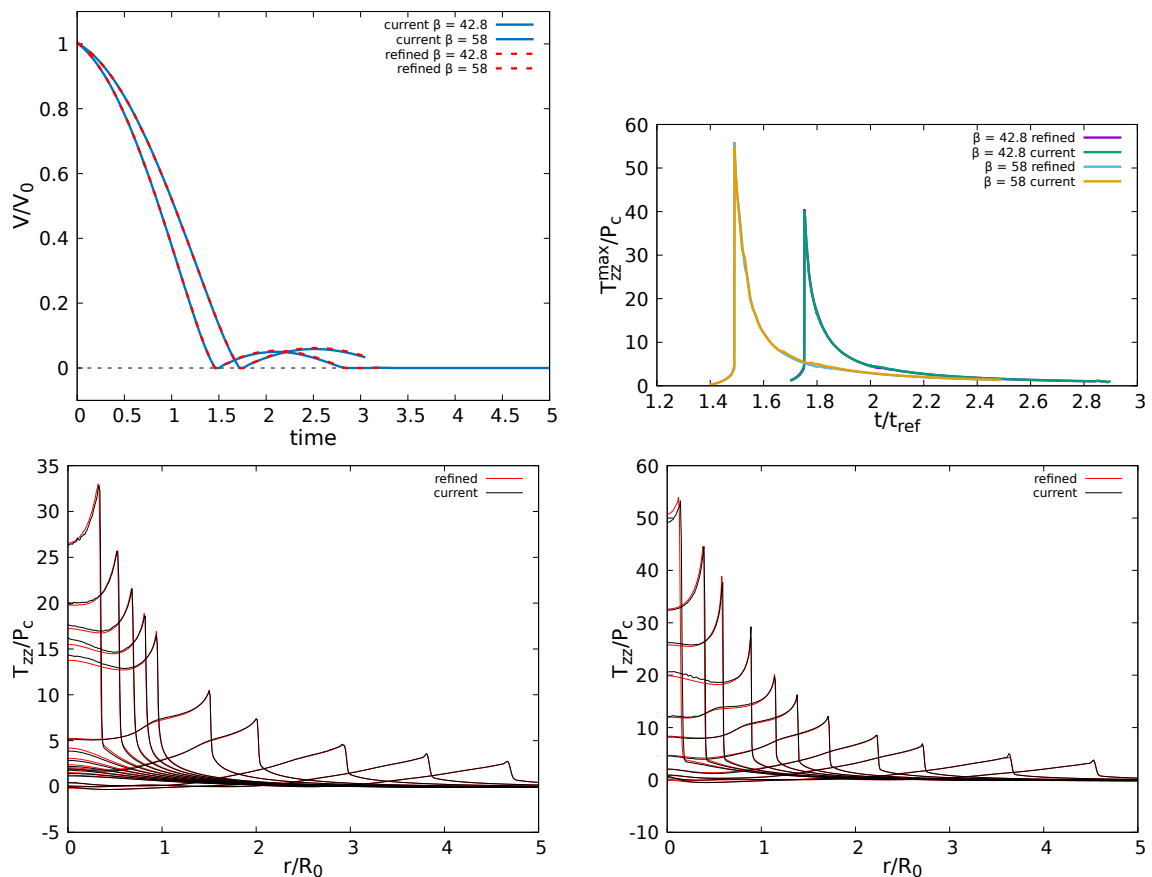
3

Figure 3: Top Left: Volume vs time comparison for the two cases at different maximum resolution. Top Right: Maximum stress at the wall vs time, for the two cases at different maximum resolution. Bottom: Pressure fields at the wall vs radial distance from the axis of symmetry. Comparison between the two simulations at different maximum resolution. Left: $\beta = 42.8$, $s = 1.2$. Right: $\beta = 58$, $s = 1.2$.

# 2 Numerical formulation for dynamic elastoplasticity

## 2.1 Weak form

The linearized momentum equation for an elastoplastic solid is (see §4 in the manuscipt)

$$\rho_s \frac{\partial^2 \mathbf{r}}{\partial t^2} = \nabla \cdot \boldsymbol{\sigma}, \tag{S18}$$

to be solved in the cylindrical domain $\Omega_s = [0, L/2] \times [0, 2\pi] \times [-H_s, 0]$, with boundary conditions

$$\boldsymbol{\sigma} \hat{\mathbf{n}} = \boldsymbol{\sigma} \hat{\mathbf{e}}_z = T_{zz} \hat{\mathbf{e}}_z, \qquad \text{at} \qquad z = 0. \tag{S19}$$

Using the following notation to shortly indicate the integral of the product of two functions over the simulation domain,

$$(f, g)_{\Omega_s} = \int_{\Omega_s} fg \, \mathrm{d}\mathbf{x}, \tag{S20}$$

denoting with $\mathbf{a}$ the acceleration $\mathbf{a} = \partial^2 \mathbf{r} / \partial t^2$, and choosing appropriate test functions $\boldsymbol{\phi}$ to satisfy the BC, the weak form of equation (S18) is

$$\rho_S (\mathbf{a}, \boldsymbol{\phi})_{\Omega_s} + (\boldsymbol{\sigma}, \nabla \boldsymbol{\phi})_{\Omega_s} - (T_{zz} \hat{\mathbf{e}}_z, \boldsymbol{\phi})_{\partial \Omega_s} = 0. \tag{S21}$$

To solve it numerically, we need to adopt appropriate temporal and spatial discretizations, and to treat nonlinearities arising due to plasticity.

Equation (S21) is solved within a time interval $t \in [0, t_f]$, which is uniformly subdivided in $N$ timesteps $[t_n, t_{n+1}]$ such that $t_{n+1} = t_n + \Delta t$, with $\Delta t = t_f / N$. The time step adopted allows the
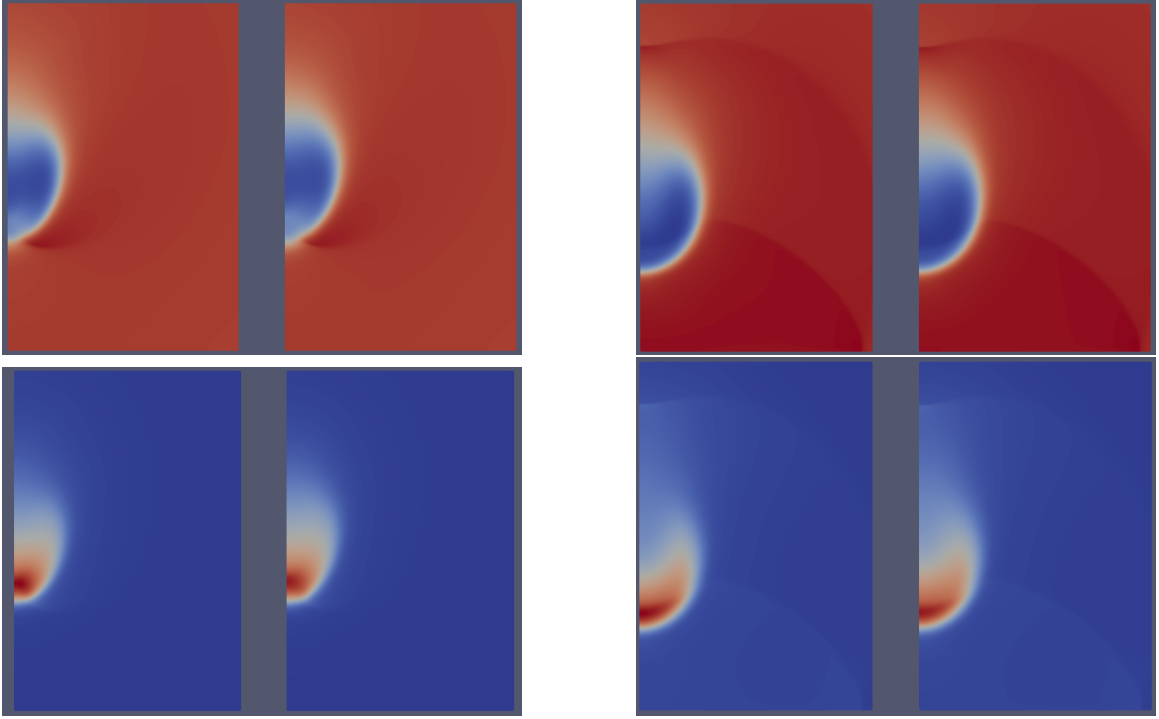
4

Figure 4: Top: Density comparison. Left panel, $t/T_c^w < 1$ - coarse grid, $\Delta_{min} = L/2^{15}$, left side and fine grid, $\Delta_{min} = L/2^{16}$, right side of the left panel. Right panel, $t/T_c^w > 1$ - coarse grid, left side and fine grid, right side of the right panel. Bottom: Corresponding temperature comparison.

resolution of the fastest timescale in the system The temporal scheme adopted in this work is an implicit Newmark $\beta$-method [1, 3]. Displacement, velocity and acceleration fields are computed as follows:

$$\mathbf{r}_{n+1} = \mathbf{r}_n + \Delta t \mathbf{v}_n + \left(\frac{1}{2} - \beta\right) \Delta t^2 \mathbf{a}_n + \beta \Delta t^2 \mathbf{a}_{n+1} = \hat{\mathbf{r}}_{n+1} + \beta \Delta t^2 \mathbf{a}_{n+1}, \tag{S22}$$

$$\mathbf{v}_{n+1} = \mathbf{v}_n + (1 - \gamma)\Delta t \mathbf{a}_n + \gamma \Delta t \mathbf{a}_{n+1} = \hat{\mathbf{v}}_{n+1} + \gamma \Delta t \mathbf{a}_{n+1}, \tag{S23}$$

where $\beta$ and $\gamma$ are constant parameters that can be tuned in order to obtain different behaviours out of the scheme, such as energy conservation or dissipation at high frequencies [5]. In this work, we chose to select $\beta = 0.49$ and $\gamma = 0.9$ Thus, the time derivative in (S18) can be expressed as

$$\mathbf{a}_{n+1} = \left.\frac{\partial^2 \mathbf{r}}{\partial t^2}\right|_{n+1} \approx \frac{\mathbf{r}_{n+1} - \hat{\mathbf{r}}_{n+1}}{\beta \Delta t^2}. \tag{S24}$$

Since the problem in (S21) is nonlinear due to plasticity effects, an iterative procedure is needed. We decided to adopt a Newton-Raphson iteration scheme, with residual

$$\Psi_{n+1} = \rho_S \left(\mathbf{a}_{n+1}, \boldsymbol{\phi}\right)_{\Omega_s} + \left(\boldsymbol{\sigma}_{n+1}, \nabla \boldsymbol{\phi}\right)_{\Omega_s} - \left(T_{zz}^{n+1}\hat{\mathbf{e}}_z, \boldsymbol{\phi}\right)_{\partial\Omega_s}$$
$$= \frac{\rho_S}{\beta \Delta t^2}\left(\mathbf{r}_{n+1} - \hat{\mathbf{r}}_{n+1}, \boldsymbol{\phi}\right)_{\Omega_s} + \left(\boldsymbol{\sigma}_{n+1}, \nabla \boldsymbol{\phi}\right)_{\Omega_s} - \left(T_{zz}^{n+1}\hat{\mathbf{e}}_z, \boldsymbol{\phi}\right)_{\partial\Omega_s}, \tag{S25}$$

and then linearize it around the $k$-th iteration and solve for the subsequent equation to be equal to zero,

$$\Psi_{n+1}^{k+1} \approx \Psi_{n+1}^k + \left.\frac{\partial \Psi}{\partial \mathbf{r}}\right|_{n+1}^k (\mathbf{r}_{n+1}^{k+1} - \mathbf{r}_{n+1}^k) = 0, \tag{S26}$$

i.e. find the incremental solution $\delta \mathbf{r}_{n+1}^k = \mathbf{r}_{n+1}^{k+1} - \mathbf{r}_{n+1}^k$ that satisfies

$$\left.\frac{\partial \Psi}{\partial \mathbf{r}}\right|_{n+1}^k \delta \mathbf{r}_{n+1}^k = -\Psi_{n+1}^k. \tag{S27}$$

5

Writing down (S27) explicitly results in

$$
\left(\delta \mathbf{r}_{n+1}^k, \boldsymbol{\phi}\right)_{\Omega_s} + \frac{\beta \Delta t^2}{\rho_S} \left( \left.\frac{\partial \boldsymbol{\sigma}}{\partial \mathbf{r}}\right|_{n+1}^k \delta \mathbf{r}_{n+1}^k, \nabla \boldsymbol{\phi} \right)_{\Omega_s} =
$$
$$
- \left[ \left(\mathbf{r}_{n+1}^k - \hat{\mathbf{r}}_{n+1}, \boldsymbol{\phi}\right)_{\Omega_s} + \frac{\beta \Delta t^2}{\rho_S} \left(\boldsymbol{\sigma}_{n+1}^k, \nabla \boldsymbol{\phi}\right)_{\Omega_s} - \frac{\beta \Delta t^2}{\rho_S} \left(T_{zz}^{n+1}\hat{\mathbf{e}}_z, \boldsymbol{\phi}\right)_{\partial\Omega_s} \right], \qquad \text{(S28)}
$$

where one should notice that $\hat{\mathbf{r}}_{n+1}$ and $T_{zz}^{n+1}\hat{\mathbf{e}}_z$ are known at each timestep. The source of nonlinearity in (S28) is the integral involving the stress tensor, which carries information about plasticity occurring in the material.

The spatial discretization adopted in this work considers the simulation domain $\Omega_s$ as composed of $N_{cells}$ non-overlapping cells $\Omega_s^h$ which are sufficient to cover the whole domain, $\Omega_s = \cup^{N_{cells}}\Omega_s^h$. The computational domain is composed of uniformly spaced cells arranged in a $2048 \times 2048$ structured grid, with spacing $\Delta = L/2/2048$ ($L = 20R_0$), this being sufficient to accurately resolve the solid dynamics. To prevent spurious reflections at the boundary of the computational domain, Rayleigh damping layers are introduced. In these layers, which occupy a region at the boundaries $r = R$ and $z = -H_s$ of $\Omega_s$, the equations are modified by adding the artificial term $-\alpha\dot{\mathbf{r}}$ to the right-hand side. The thickness and damping coefficient of these layers were adjusted to ensure that waves are dissipated before they can reflect back into the physically relevant region. On each cell, the test functions $\boldsymbol{\phi}$ take the form of appropriate shape functions. In the present work, piecewise linear shape functions are adopted, and we assume that it is possible to represent the solution $\mathbf{r}(\mathbf{x}, t)$ as a linear combination of the shape functions through the nodal values $\tilde{\mathbf{r}}_i(t)$, such that

$$
\mathbf{r}(\mathbf{x}, t) = \sum_i^{n_{nodes}} \tilde{\mathbf{r}}_i(t)\phi_i(\mathbf{x}), \qquad \text{(S29)}
$$

$$
\nabla \mathbf{r}(\mathbf{x}, t) = \sum_i^{n_{nodes}} \tilde{\mathbf{r}}_i(t)\nabla\phi_i(\mathbf{x}). \qquad \text{(S30)}
$$

Substituting (S29) in (S28) gives the following,

$$
\left[ \left(\phi_i, \phi_j\right)_{\Omega_s^h} + \frac{\beta \Delta t^2}{\rho_S} \left( \left.\frac{\partial \boldsymbol{\sigma}}{\partial \boldsymbol{\epsilon}}\right|_{n+1}^k \nabla\phi_i, \nabla\phi_j \right)_{\Omega_s^h} \right] \delta\tilde{\mathbf{r}}_{n+1,i}^k =
$$
$$
- \left[ \left(\mathbf{u}_{n+1}^k - \hat{\mathbf{r}}_{n+1}, \phi_j\right)_{\Omega_s^h} + \frac{\beta \Delta t^2}{\rho_S} \left(\boldsymbol{\sigma}_{n+1}^k, \nabla\phi_j\right)_{\Omega_s^h} - \frac{\beta \Delta t^2}{\rho_S} \left(T_{zz}^{n+1}\hat{\mathbf{e}}_z, \phi_j\right)_{\partial\Omega_s^h} \right], \qquad \text{(S31)}
$$

that can now be solved to find $\delta\tilde{\mathbf{r}}_{n+1}^k$. In (S31), the elastoplastic consistent tangent tensor appears,

$$
\mathbf{C}_{n+1}^{ep\,k} = \left.\frac{\partial \boldsymbol{\sigma}}{\partial \boldsymbol{\epsilon}}\right|_{n+1}^k, \qquad \text{(S32)}
$$

which is the algorithmic counterpart of the elastoplastic tensor.

Solving the problem (S31) provides the incremental displacement $\delta\tilde{\mathbf{r}}_{n+1}^k$, that can be used to update the global solution vectors of displacement, acceleration and velocity,

$$
\mathbf{r}_{n+1}^{k+1} = \mathbf{r}_{n+1}^k + \delta\tilde{\mathbf{r}}_{n+1}^k, \qquad \text{(S33)}
$$

$$
\mathbf{a}_{n+1}^{k+1} = \frac{1}{\beta\Delta t^2}(\mathbf{r}_{n+1}^{k+1} - \hat{\mathbf{r}}_{n+1}), \qquad \text{(S34)}
$$

$$
\mathbf{v}_{n+1}^{k+1} = \hat{\mathbf{v}}_{n+1} + \gamma\Delta t\,\mathbf{a}_{n+1}^{k+1}. \qquad \text{(S35)}
$$

The above procedure is then repeated each iteration, until the residual computed at the $m$-th iteration is lower than a certain prescribed value,

$$
\left\| \Psi_{n+1}^m \right\| \leq \epsilon \left\| \Psi_{n+1}^1 \right\|, \qquad \text{(S36)}
$$

where $\epsilon$ is a sufficiently small specified tolerance. Once the convergence criterion (S36) is satisfied, the corresponding displacement is accepted as the solution at the new timestep $t_{n+1}$.

$$
\mathbf{r}_{n+1} = \mathbf{r}_{n+1}^m
$$

All solution vectors are then updated and a new initial guess is made to solve the problem at the subsequent timestep. Usually, the initial guess for displacement is taken as the converged value of the displacement vector,

$$\mathbf{r}_{n+1}^1 = \mathbf{r}_n,$$

and the initial guesses for velocity and acceleration follow from (S35) and (S34).

Within a single Newton-Raphson iteration, that occurs only in the case of local plasticity activating in the material due to local exceeding of the yield criterion, the return mapping algorithm [2, 4] is employed, which is an elastic-predictor/plastic-corrector algorithm that iteratively calculates the local plastic flow and updates the plasticity variables and the value of the elastoplastic tangent operator Eq. (S32), that is used in the system of discretised Eqs. (S31).

# References

[1] Nathan M Newmark. "A method of computation for structural dynamics". In: *Journal of the engineering mechanics division* 85.3 (1959), pp. 67–94.

[2] Juan C Simo and Robert Leroy Taylor. "Consistent tangent operators for rate-independent elastoplasticity". In: *Computer methods in applied mechanics and engineering* 48.1 (1985), pp. 101–118.

[3] Olek C Zienkiewicz and Robert L Taylor. *The finite element method for solid and structural mechanics*. Elsevier, 2005.

[4] Juan C Simo and Thomas JR Hughes. *Computational inelasticity*. Vol. 7. Springer Science & Business Media, 2006.

[5] Thomas JR Hughes. *The finite element method: linear static and dynamic finite element analysis*. Courier Corporation, 2012.

[6] Daniel Arndt et al. "The `deal.II` Library, Version 9.5". In: *Journal of Numerical Mathematics* 31.3 (2023), pp. 231–246. DOI: 10.1515/jnma-2023-0089. URL: https://dealii.org/deal95-preprint.pdf.